Available online at www.sciencedirect.com
ScienceDirect
Journal of the European Ceramic Society 30 (2010) 847–855
www.elsevier.com/locate/jeurceramsoc

Plasma-scan sintering of aluminosilicate sol–gel films

J. Gao [a], T. Zhang [b,*], Y. Bao [a], D.T. Gawne [a]

[a] *Department of Engineering Systems, London South Bank University, London, SE1 0AA, UK*
[b] *Faculty of Engineering, Kingston University, London, SW15 3DW, UK*

Received 26 July 2009; received in revised form 27 September 2009; accepted 1 October 2009
Available online 5 November 2009

Abstract

The high temperatures and velocities of plasma jets give them uniquely high heat transfer coefficients and the ability for extremely rapid heat transfer. These characteristics have been applied to use plasma scanning to sinter aluminosilicate films prepared by sol–gel processing. The critical thickness, up to which crack-free films can be obtained, was found to be significantly lower for plasma-scan sintering than for conventional furnace sintering. However, crack-free films above the critical thickness were produced by multiple dipping to produce individual layers below the critical thickness and plasma scanning after each dip. Multilayered aluminosilicate films deposited on steel substrates and plasma-scan sintered for 3 min at 600 °C showed the same microstructure and scratch resistance as that of conventionally furnace-sintered films after 60 min at 600 °C. A process model has been developed for the plasma-scan sintering process that can predict temperature profiles within the film–substrate system and form a basis for process control.

Keywords: Plasma sintering; Sol–gel film; Nano film; Fast sintering

1. Introduction

Ceramic thin films have a wide range of applications in optics, electronics, catalysis and corrosion protection.[1–3] The sol–gel processing route is particularly attractive for fabricating ceramic films, since the liquid precursor can be readily applied to a substrate by spinning, dipping or spraying. There are several practical advantages of the sol–gel technique including low-temperature processing, continuous deposition on large-area substrates under ambient conditions, high purity and homogeneity, and unique combinations of coating-substrate properties. There are two principal sol–gel processing routes for oxide ceramics: (i) gelation of a particulate aqueous dispersion of hydrated oxides (sol) by removal of water, or (ii) crosslinking of inorganic polymers by hydrolysis of metal alkoxides in an alcoholic solvent. For both routes, the final conversion to the oxide is accomplished by heat-treating the gel. Another factor common to both routes is the large shrinkage that takes place in two stages of processing: during the drying of the gel and during the sintering of the gel to form a dense ceramic. This shrinkage induces tensile stresses in the film, which often cause cracking and delamination of the film, so that it is difficult to produce thick ceramic films by sol–gel processing. However, thick ceramic films have been prepared without surface cracking by stacking films using repeated spin- or dip-coating and firing processes.[4–7] Experimental work has shown that the sintering parameters play an important role in the evolution of film properties in the sol–gel route.[8–9] In order to make the fabrication of multilayer films more efficient and avoid degrading their properties, each heating and firing should be as short as possible. The use of furnaces, laser light, ion beam, ultra-violet irradiation and microwave-assisted sintering to densify sol–gel films has been studied by a number of groups over the past twenty years.[10–13] However, there are no reports on the use of plasma jets in combination with sol–gel processing to produce dense ceramic films. Since the plasma jet provides very high temperatures and heat transfer coefficients, it can provide much faster heating compared with the methods mentioned above. It is also expected that the fast heating will be able to generate large temperature differences between the film and substrate, particularly when thick or low thermal conductivity materials are used as substrates. This will save considerable energy, especially for multilayer sintering, as it will avoid the need to heat the entire substrate. The main objective of this paper is to study

* Corresponding author.
E-mail address: t.zhang@kingston.ac.uk (T. Zhang).

0955-2219/$ – see front matter © 2009 Elsevier Ltd. All rights reserved.
doi:10.1016/j.jeurceramsoc.2009.10.003

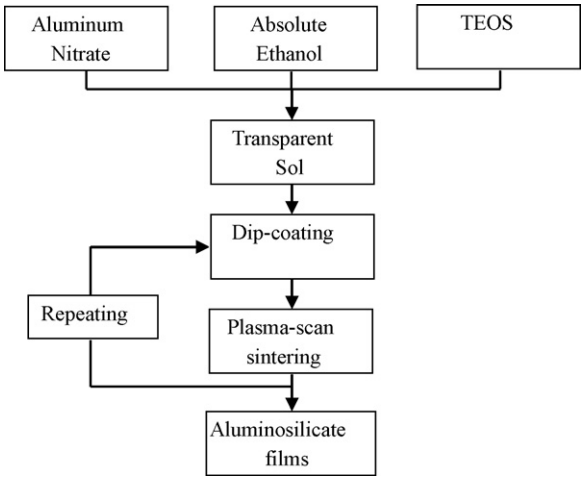

Fig. 1. Flow chart showing sol–gel processing and plasma-scan sintering of aluminosilicate films.

the use of a plasma jet as a heat source for treating sol–gel films and its effect on film properties. Computer simulations were carried out in comparison with the experimental results to help understand the interaction of the plasma with the film–substrate combination and form a basis for process control.

2. Experimental procedure

A flow diagram showing the film preparation through sol–gel processing followed by plasma-scan sintering is outlined in Fig. 1. The starting materials were tetraethyl orthosilicate (TEOS), aluminum nitrate nanohydrate ($Al(NO_3)_3 \cdot 9H_2O$), and absolute ethanol. Aluminum nitrate nanohydrate was first dissolved in absolute ethanol and then mixed in the ratio of 3Al:Si, with TEOS (the stoichiometric composition of mullite). The mixed solution was stirred for 3 h at the temperature of 80 °C to obtain a transparent sol. The concentration of the solution was adjusted to 0.1 M with ethanol. Stainless steel of dimensions of 50 mm × 25 mm × 1.5 mm was used as the substrates for the aluminosilicate film. The surface of the stainless steel was ground with SiC paper grade P2400, cleaned with detergent and rinsed with acetone in an ultrasonic bath. The roughness of the substrate was 0.08 μm (Ra) after grinding with abrasive paper. The coating was applied by a wet dipping technique in which the prepared substrates were dipped into the aged sol at a constant rate of 6 cm/min and withdrawn at the same speed. The coated samples were dried initially at room temperature for 120 min before the final drying at 110 °C for 30 min.

The coated samples were densified by sintering using both plasma-scan and conventional furnace. Scanning was carried out with a Sulzer-Metco plasma-spray system using an MBN torch and MCN control unit. The plasma conditions used are summarized in Table 1.

The temperatures of the coated substrate were measured during the plasma-scan sintering using a high-performance non-contact thermometer MX4 (Raytek, UK). The data recoding time was set as 0.1 s. For comparison, some of the coated samples were sintered at 600 °C for 1 h in air in a furnace with a heating rate of 5 °C min^{-1}.

Table 1
Plasma process parameters.

Argon flow rate ($l\,min^{-1}$)	50	50
Hydrogen content (%)	2	6
Current (A)	450	450
Spraying distance (mm)	85	85

Scratch resistance of the films was assessed using a Teledyne Taber shear/scratch tester. A conical diamond indenter with an apex angle of 120° was used with a sliding velocity of 5 mm/s to produce a single scratch of length 10 mm. The applied loads were in the range of 0.10–0.70 N. The widths of the scratch trace under different applied loads were measured using optical microscope.

The corrosion tests were performed using an EG&G M6310 Electrochemical Analyzer. Solution containing 3.5% NaCl in deionized water was used as the electrolyte. An Ag/AgCl electrode was used as the reference electrode and platinum as the counter electrode. The oxidation resistance of the coated substrate was evaluated by measuring the increase in weight of the samples after isothermal heating in air at 900 °C for times between 2 and 20 h. The cross-section of the coated sample was polished and then etched using aqueous hydrochloric acid. The microstructure of the samples was observed with optical microscopy and scanning electron microscopy (S-4300SE, Hitachi Co. Ltd). IR spectroscopic measurement was performed using a Fourier transform infrared spectrometer (Satellite FT-IR, Mattson, USA).

3. Results and discussion

3.1. Plasma-scan sintering and process modelling

Plasma-scan sintering involves the repeated scanning of the coated substrate with a high-temperature, high-velocity plasma jet. During the scanning operation, the distance between the intersection of central axis of the plasma jet with the substrate and any position P on the substrate surface varies as the plasma torch moves across the substrate as shown schematically in Fig. 2. The temperature immediately above the point P on the substrate, therefore, varies with the distance of point P from the central axis of the plasma jet. This temperature governs the

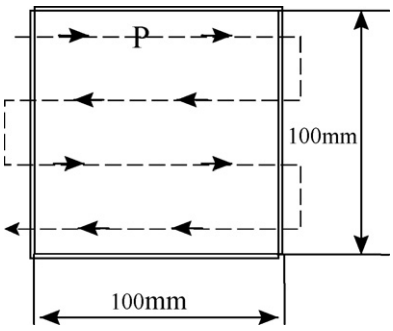

Fig. 2. Schematic of plasma-jet scanning of a solid substrate.

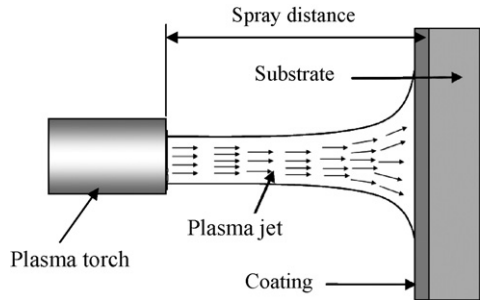

Fig. 3. Schematic of impinging plasma jet on a solid substrate.

heat transfer from the plasma jet to the substrate and thus determines the surface temperature profile of the coated component. The temperature profile of the component during scanning is critical for the densification, the structure and its properties. To achieve satisfactory process control, a full understanding of the temperature profile is necessary. However, it is difficult to measure experimentally the temperature in the film accurately, because the film is very thin, the plasma jet moves rapidly and contains large temperature gradients. For this reason, computer simulation was carried out.

When the plasma jet impinges on the substrate, it flows out to the sides in a radial manner as shown in Fig. 3. As a result, the substrate does not experience the plasma as a uniform-temperature beam but as a diffuse flow of hot gas jet over its surface in which the gas velocity and temperature gradually decrease with distance from the jet centre. The authors have used a computational fluid dynamics (CFD) package to simulate the temperature profiles of the plasma impinging on a solid substrate along the axial and radial dimensions of the jet. The computational method, which has been explained previously by the authors,[14,15] is employed to calculate the temperature of a moving plasma jet above a fixed point. Fig. 4a shows the calculated plasma jet temperature immediately above the point P on the substrate surface during plasma scanning (for a plasma gas composition of 2% hydrogen in argon, the gas flow rate is 50 standard litres per minute). The results indicate drastic temperature variations in the plasma gas temperature immediately above a fixed point P on the substrate surface. Fig. 4b shows that this temperature spiking is due to the scanning movement of the jet, which causes sharp fluctuations in distance between P and central axis of the plasma jet.

The temperature of the substrate subjected to the scanning action of the plasma jet (as shown in Fig. 3a) can be calculated. The substrate used in the calculation is a 100 mm × 100 mm stainless steel plate of thickness 1.5 mm and this is coated with a layer of aluminosilicate coating of thickness 1 μm. The spraying distance (the axial distance from the torch nozzle to the substrate as shown in Fig. 3) is 80 mm. Other assumptions made for the calculation are: (i) the heat transfer in the coated substrate is one-dimensional since its thickness is two orders of magnitude less than its length and width; (ii) the scanning speed of the plasma jet is 100 mm/s; (iii) the vertical gap between each horizontal pass is 25 mm. (The torch returns, therefore, to a given point after four passes in approximately 4 s as indicated in Fig. 4b.)

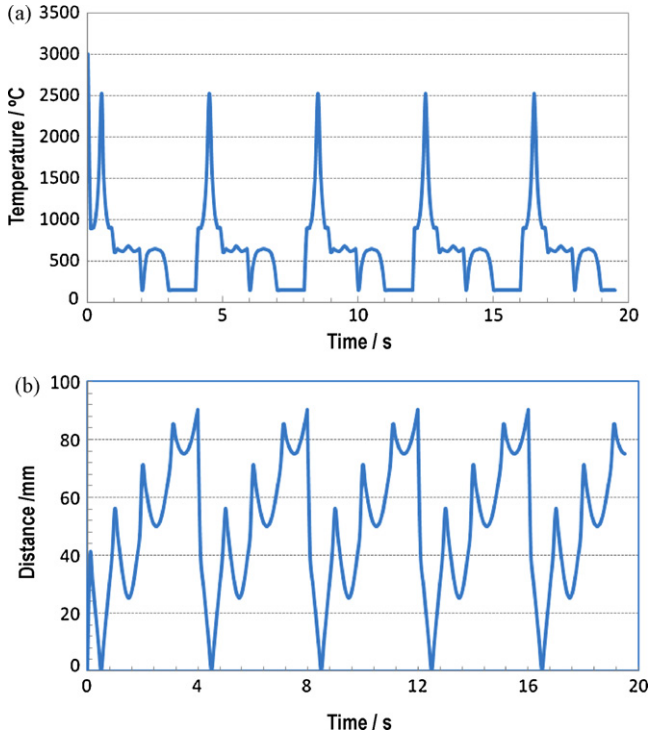

Fig. 4. (a) Calculated plasma-jet temperature immediately above a fixed point P on the substrate surface during plasma scanning. (b) Calculated distance of the plasma jet centre from a fixed point P on substrate as a function of time.

Based on these assumptions, the governing equation for the heat transfer in the coating and substrate can be expressed as:

$$\frac{\partial^2 T}{\partial z^2} = \frac{1}{D}\left(\frac{\partial T}{\partial t}\right) \tag{1}$$

where T is the temperature within the film or substrate at a distance z from the cold face of the substrate (or back of the substrate). The thermal diffusivities D are assumed to be constants for the substrate and coating respectively. At the boundary between the substrate and the coating, a combined element is considered.[14,15] At the film surface, the elements are subjected to the impinging plasma jet. The heat transfer from the plasma jet to the substrate is given as:

$$q = h(T_p - T_s) \tag{2}$$

where q is the total heat flux from the plasma jet to the substrate and h is the convective heat transfer coefficient. T_p and T_s are temperatures of the plasma jet and the top surface of the coating respectively. The radiative transfer from the plasma to the substrate is not considered here as the work done by Nylen et al.[16] showed that it could be neglected. Since the film is an amorphous glass, no latent heat changes were considered in the calculations. The heat transfer coefficient h at the surface of the film is a dynamic value which is a function of the position relative to the centre of the plasma jet, whereas its value at the back of substrate is taken as a constant for a natural wall condition. A more detailed description of the computational model may be found in previous publications.[17,18]

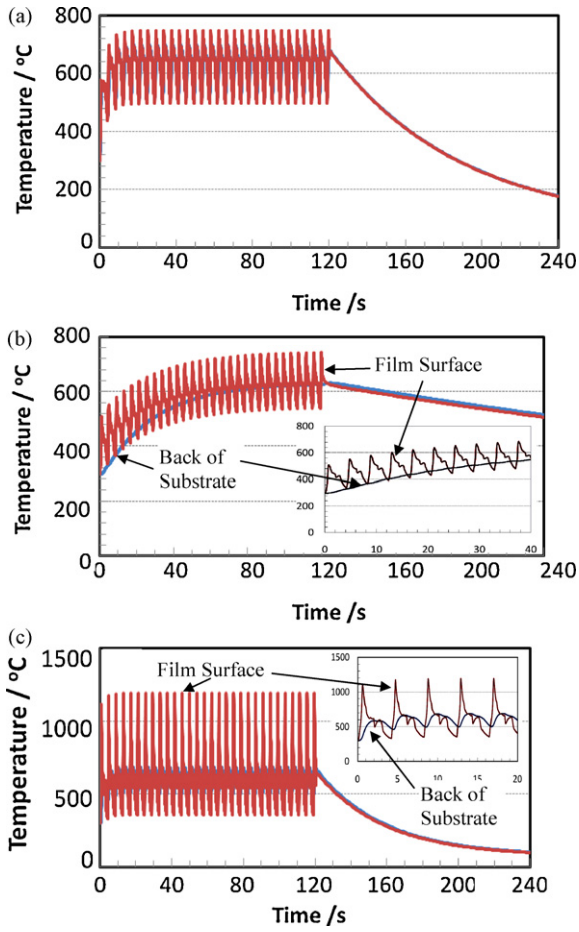

Fig. 5. Calculated temperatures at film surface and at the back of the substrate during plasma scanning for coating thickness 1 μm; (a) stainless steel substrate 1.5 mm, (b) stainless steel substrate 10 mm and (c) glass substrate 1.5 mm.

Fig. 5 shows the calculated temperature at the top surface of the film and that at the back of the substrate during plasma scanning. The film and substrate experience large temperature fluctuations or oscillations due to the rapid scanning movement of the jet and its large temperature gradients. In all cases, the temperature of the film surface is predicted to increase very rapidly in the first second, since the centre of the plasma jet (where the gas temperature and heat transfer coefficient are both very high) moves towards Point P (Fig. 2). As scanning continues, the temperature difference between the coating and the plasma gas at P reduces and the rate of the temperature increases is reduced. After four complete scans (about 20 s), the coating temperature rises no more and a thermal equilibrium is reached. This temperature can be defined as the equilibrium sintering temperature of plasma-scan sintering under specified conditions.

In Fig. 5a, the temperature of the film and substrate are very similar and so the curves overlap, because the low thickness (1.5 mm) and high conductivity of substrate generate a very low-temperature gradient. However, when substrate is much thicker (10 mm) as shown in Fig. 5b, there is a large temperature difference between the film surface and the back of the substrate and so the individual curves can now be resolved. The inset in Fig. 5b shows a magnified view of the curves over the first 20 s: the smoothly rising curve indicates the temperature at the back of the substrate, while the oscillating curve shows the temperature of the film surface. The temperatures of the film and substrate rise more slowly in the 10 mm thick substrate compared with the 1.5 mm thick substrate. This is due to the 'heat sink' effect of the large thermal mass of the thicker substrate. Fig. 5a and b show that a further consequence of the heat sink effect of thick substrates is an extended time to reach the equilibrium sintering temperature.

Surprisingly, the inset in Fig. 5b shows that after 15 s, the temperature of the back of the substrate rises above the lowest temperature of the film surface. This is because the gas temperature above the film surface at P at 15 s is now lower than the substrate temperature (Figs. 4a and 5b) when the centre of plasma jet is far away from point P. As a result, the plasma gas stream (emanating laterally from the jet as shown in Fig. 3) is now cooling the film surface. Owing to the high velocity of the plasma jet, the heat transfer coefficient between plasma jet and film is very high and so the cooling is rapid at the film surface. This contrasts with the cooling at the back of the substrate where ambient conditions with a consequent low heat transfer coefficient resulting in a much lower tendency for cooling.

The results from the computational model show that during each pass of the torch, the plasma jet produces a thermal shock to the surface and this generates a rapid temperature rise in the film. This brings about important savings in energy. Conventional sintering in a furnace requires heating the entire charge or furnace contents so that they reach thermal equilibrium at the sintering temperature and this clearly needs a much longer time than plasma-scan sintering. Besides saving time and raising productivity, plasma scanning does not need to raise the temperature of the substrate, walls and hardware in the furnace. The film can be sintered effectively without heating the entire substrate to an equilibrium temperature. This advantage of directing most of the energy to heat the film where it is needed rather than the substrate may be controlled by the adjusting of plasma input power, scanning distance and speed to increase the temperature difference between the film and substrate. This contrasts with conventional sintering in a furnace, where most of the energy is used to heat the substrate and furnace hardware.

Films fabricated by the sol–gel route using conventional furnace sintering are typically microporous due to the evaporation of the solvent. It is known that the porosity of the film can be reduced by raising the sintering temperature[19] but such high temperatures can cause oxidation and distortion of the substrate. Plasma-scan sintering has the ability to reduce this problem, as it does not need to heat the entire substrate to high temperatures.

Fig. 5c shows an important result: when a low thermal conductivity material, such as glass, is used as a substrate, a much larger temperature difference between the film and substrate is achieved than that for steel in Fig. 5a. The temperature at the back of the substrate is 600 °C while the peak temperature at film is as high as 1200 °C. This is of practical significance since many thermally activated processes like sintering following the Arrhenius behaviour: the reaction rates generally increase rapidly with increasing temperature and the amount of reaction, or sintering in this case, at each temperature interval is additive. The

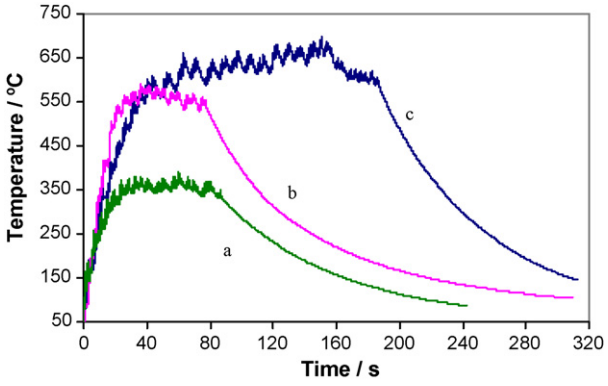

Fig. 6. Measured temperature traces at the surface of aluminosilicate films during plasma-scan sintering under various plasma gas compositions: (a) 1 min scan with argon + 2% hydrogen; (b) 1 min scan with argon + 6% hydrogen and (c) 3 min scan with argon + 6% hydrogen.

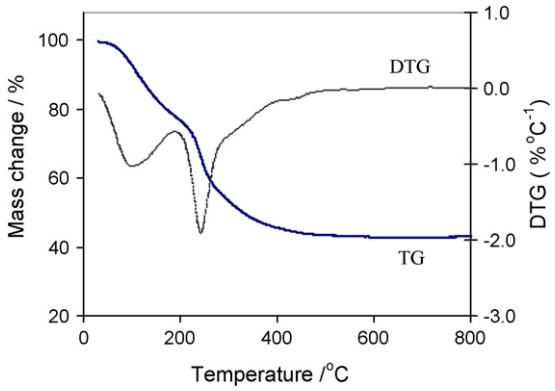

Fig. 7. Thermogravimetric (TG) curve and corresponding derivative (DTG) curve of the aluminosilicate gel.

high temperatures reached in plasma scanning will therefore accelerate the sintering process.

3.2. Model validation and sintering control

The temperature of the aluminosilicate coated steel during the plasma-scan sintering was varied by adjusting the plasma-spray conditions. Fig. 6 gives the experimentally measured temperatures at the film surface under three plasma conditions: (a) a 1-min scan with an argon–2% hydrogen plasma, (b) a 1-min scan with an argon–6% hydrogen and (c) a 3-min scan with argon–6% hydrogen. Since the aluminosilicate film is only 1 μm thick and the steel substrate is 1.5 mm thick, the substrate temperature is expected to be very close to the film temperature, as predicted in Fig. 5a. The oscillations of the temperature in Fig. 6 are the consequence of the movement of the plasma torch. The temperatures measured during plasma scanning were found to be similar to and follow the same trends as those predicted. However, the temperature fluctuations were not as great as those predicted in Fig. 5. This is attributed to: (i) the response time of the thermometer is 0.1 s, during this time the plasma jet has traveled 10 mm, which means that the gas temperature above the measurement point has changed (Fig. 3) so the film temperature has changed; (ii) the recorded temperature is the average temperature over the measurement spot. The spot size is 6 mm, this means that the measured film temperature was an average temperature of 6 mm spots within 0.1 s, rather than real time temperature for a fixed point as described in computer simulation. However, Fig. 6 indicates that the temperature of the coated substrate rise rapidly initially and then reaches an equilibrium temperature (the plasma-sintering temperature). At the end of scanning, the coated substrate cools down at a much slower rate. This behaviour is consistent with the predictions of the model as given in Fig. 5. In particular, the measured equilibrium temperature is close to the predicted equilibrium temperatures (Fig. 5a).

The temperature and time are the most important parameters to be controlled in conventional sintering and this is also the case in plasma-scan sintering. The results in Fig. 6 show that the equilibrium temperature of the coated substrate increases significantly with increasing hydrogen content of the plasma gas for a given input current (Table 1). The addition of hydrogen to argon in the plasma gas is known to increase both the heat transfer coefficient and the plasma gas temperature, which will result in increasing the film temperature. Apart from the plasma gas composition, the input arc power can also be adjusted to achieve a desired plasma temperature. The plasma-scan sintering time can be controlled by the number of scans e.g. curve (c) in Fig. 6. Scanning speed and pattern are also important parameters and can be adjusted to influence the plasma-sintering temperature and time.

3.3. Characterization of plasma-scan sintered aluminosilicate films

To determine the microstructural changes in the sintered films during plasma heating, thermogravimetric analysis (TGA) of the aluminosilicate gel was undertaken. Fig. 7 shows the TGA curves of aluminosilicate gel obtained at a heating rate of 3 °C min^{-1} in air. It indicates a significant weight loss occurred at two temperature intervals when the gel was heated from room temperature to 800 °C. The weight loss in the temperature interval of 50–210 °C is related to the loss of the bonded water during the process of esterification and the evaporation of excess ethanol. The weight loss between 210 and 460 °C is mainly due to the removal of organic compounds in the polymer silica network. No weight loss was detected above 460 °C. This information was used for the selection of the process condition, particularly in the initial heating to prevent the aluminosilicate films from cracking in the early stages. The dip-coated samples were dried at 110 °C for 30 min before plasma-scan sintering.

The infrared spectra of plasma-scan sintered and furnace-sintered aluminosilicate films are presented in Fig. 8 together with the dried but un-sintered film. It is noted that the strong vibration bands at 680, 835, 1380, and 1650 cm^{-1} (assigned to hydrocarbon bending vibrations, H_2O bending, unhydrolysed species and organic polymers, as well as to nitrate) observed in non-sintered film disappeared in the films sintered at or above 600 °C by both furnace (curve (c)) and plasma scanning (curves (d and e)). These vibration bands remained with a much lower

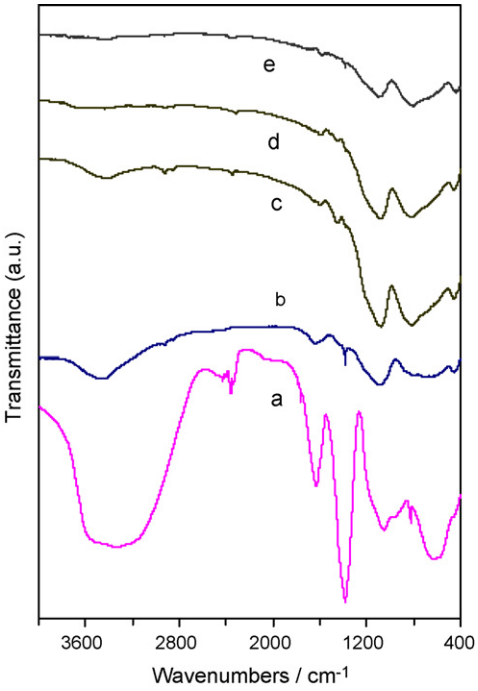

Fig. 8. Infrared spectra of aluminosilicate films: (a) without sintering; (b) sintered by plasma scan with argon + 2% hydrogen plasma; (c) sintered at 600 °C for 60 min in furnace; (d) sintered by argon + 6% hydrogen plasma for 1 min; (e) sintered by argon + 6% hydrogen plasma for 3 min.

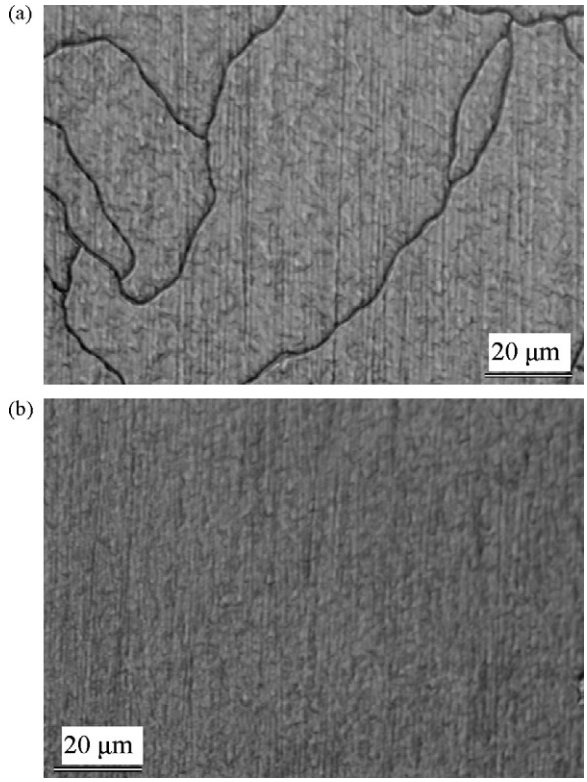

Fig. 9. Optical micrographs of the surface of aluminosilicate films prepared by two dips and then plasma-scan sintered: (a) sintered only after the second dip; (b) sintered after each dip.

strength in the films that was plasma-scanned at an equilibrium temperature of 380 °C (curve (b)). The strength of the vibration bands at 3450–3480 cm^{-1} corresponding to the hydroxyl stretching vibration has also reduced substantially in this low-temperature plasma-scanned film but completely disappeared in the films plasma-scanned at equilibrium temperatures of 600 °C and 650 °C. These observations are in good agreement with the TGA results in Fig. 7, which indicate that the combined water and organics introduced in the sol–gel stages are removed only above 460 °C.

Fig. 8 also shows that two characteristic peaks at 846 and 1108 cm^{-1} appeared in the plasma–scanned and furnace-sintered films (at 600 °C or above). These peaks are associated with aluminosilicate and so indicate that aluminosilicate films have been produced. The films became transparent after sintering by plasma-scan or furnace treatment (at 600 °C or above). It was noted that the film plasma-scanned for 1 min at 600 °C or above had the same chemical structure as the one sintered for 60 min in the furnace.

3.4. Effect of dipping sequence and plasma scanning on cracking during sintering

The computational results in Section 3.1 and experimental measurements in Section 3.2 show that during each plasma scan, the plasma torch produces a thermal shock to the surface of the coating and this results in a high temperature gradient in the coating. The benefits of rapid heating and high temperature gradients are much shorter sintering times and the potential of preventing the substrate from overheating. On the other hand, these conditions can also cause high thermal stresses, which may result in cracking of the film. The as-dipped sol–gel film contains a high proportion of organic solvents and these need to be removed in order to produce a dense inorganic film. Solvent evaporation produces a volume change of the film, which may cause microporosity and stresses even during slow furnace heating. One of the solutions to this problem is to reduce the thickness of the film subjected to plasma–scanning. The maximum thickness that can be deposited without cracking (the critical thickness) can only be determined experimentally as it is related to many factors, including sol–gel composition, preparation methods as well as dipping and plasma-sintering conditions.

The thickness of the film was controlled by the dipping rate and the number of dipping actions. Fig. 9a is an optical micrograph giving the surface of an aluminosilicate film prepared by two dips in the solution and then plasma-scanned with an argon–6% hydrogen plasma for 2 min. It shows that the film has cracked indicating that its thickness is above the critical thickness. Fig. 9b shows a crack-free surface of an aluminosilicate film. The film was also prepared by two dips but in this case, the film was plasma-scanned (for 1 min) after each dip. The total number of dips and plasma scanning time was the same in both films but scanning after each dip is therefore found to suppress cracking, as the individual layers are both below the critical thickness.

Fig. 10 gives SEM micrographs of the surfaces of aluminosilicate films prepared by three dips and then sintered by (a) argon–6% hydrogen plasma scanning for 1 min after each dip

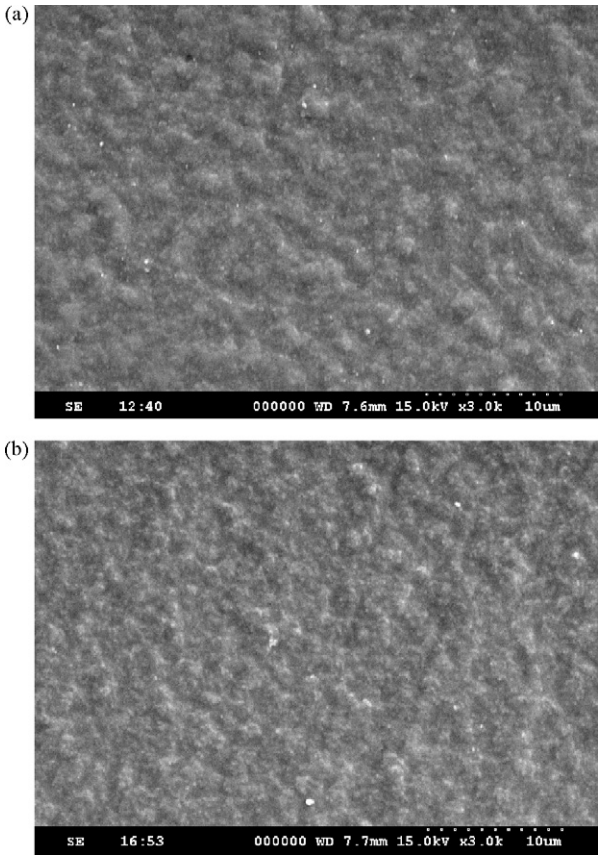

Fig. 10. SEM micrographs showing the surface of aluminosilicate films produced by three-dips and then: (a) plasma-scan sintered at 600 °C for 3 min (1 min after each dip); (b) furnace sintered at 600 °C for 60 min.

(total 3 min) and (b) furnace-sintered for 60 min after three dips and drying. The SEM micrographs reveal no microcracks in both films. The result suggests that the plasma-scan sintering produces a lower critical thickness than furnace sintering, which is attributed to its rapid heating characteristics.

Fig. 11 gives an SEM micrograph of a through-thickness fracture surface of the same aluminosilicate film as in Fig. 10a: three dips with 1 min plasma scan after each dip. The film is on the left and the etched stainless steel substrate on the right. The plasma-scan sintered film exhibits a dense, fused and featureless microstructure, which is typical of a glass. In fact, the film is expected to be glassy as the sintering temperature is too low for the formation of the mullite crystalline phase. The average film thickness was approximately 1 μm. This corresponds to a thickness for each single layer of 0.33 μm, which is the critical thickness for this material under plasma scanning.

3.5. Properties of aluminosilicate films

The scratch test enabled measurements of the width of the scratch damaged zone and the critical load at which the film detached from the substrate, which provide insight into the strength and adhesion of the films. Fig. 12 gives optical micrographs of the scratch tracks, produced by a 0.3 N applied load, on the films with and without plasma scanning. It can be seen that the width of the scratch is much narrower on the plasma-sintered

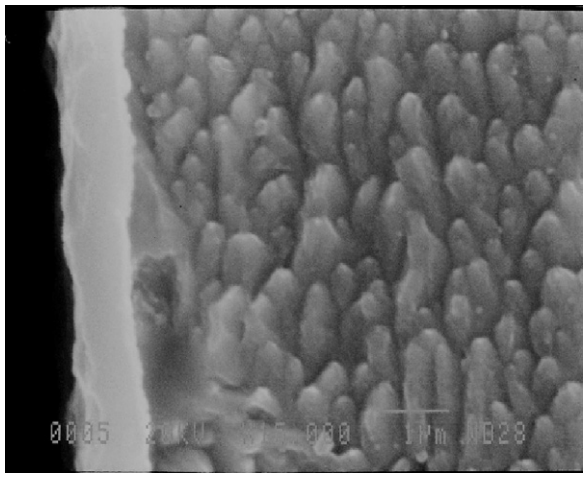

Fig. 11. SEM micrograph showing the polished and etched (with HCl) through-thickness cross-section of multilayer aluminosilicate film deposited on stainless steel and plasma-scan sintered (3 dips and plasma-scan sintered after each dip). Film on left and substrate on right.

film than that on the non-sintered film (which is completely detached from the underlying steel), indicating improved scratch resistance due to plasma-scan sintering. Fig. 13 shows the width of damaged zones measured under various applied loads for three films: (a) film before sintering, (b) film sintered in fur-

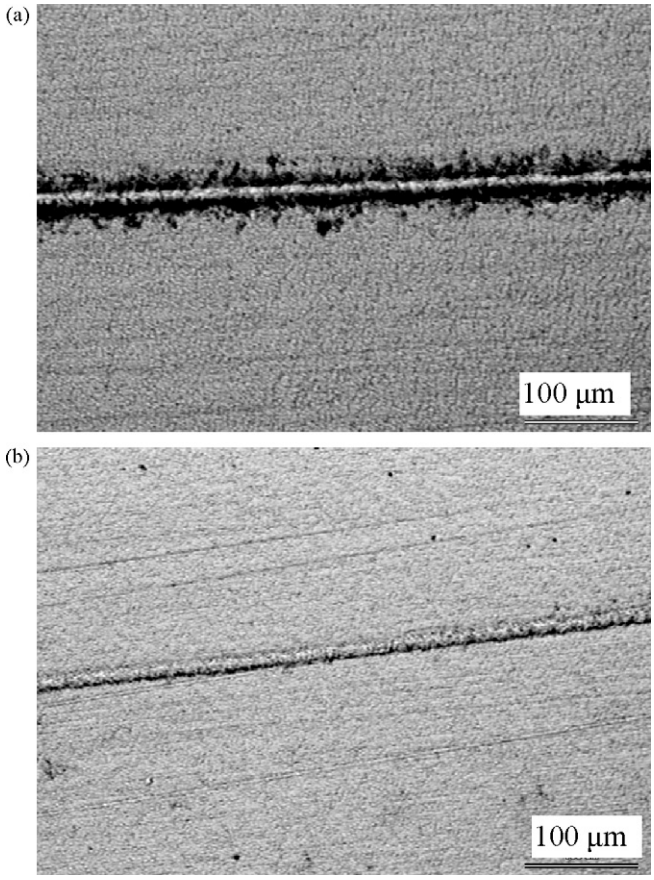

Fig. 12. Optical micrographs showing scratch traces on: (a) aluminosilicate film before sintering; (b) aluminosilicate film after plasma-scan sintering. 0.30 N applied load.

Table 2
Weight gains in uncoated stainless steel and plasma-scan sintered film on stainless steel.

	Weight increase (mg/cm^2)						
Heating time (h)	2	4	6	8	10	15	20
Coated stainless steel	0.005	0.002	0.018	0.024	0.029	0.036	0.042
Un-coated stainless steel	0.12	0.17	0.21	0.23	0.27	0.32	0.40

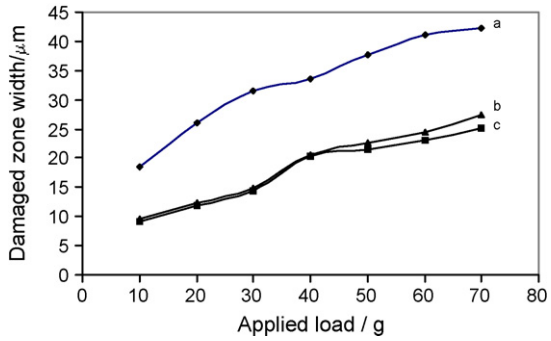

Fig. 13. Measured widths of damaged zones of scratch tracks as a function of applied load on: (a) film before sintering, (b) film sintered in furnace at 600 °C for 60 min, and (c) plasma-scan sintered film. Sintering conditions were the same as those given in Fig. 10.

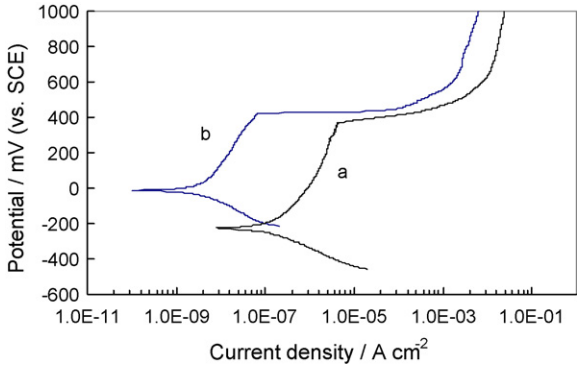

Fig. 14. Polarization curves in 3.5% NaCl for stainless steel with and without sol–gel aluminosilicate film: (a) bare uncoated stainless steel, (b) stainless steel coated with aluminosilicate film plasma-scan sintered at 600 °C for 3 min (three dips and plasma-scanned for 1 min after each dip).

nace for 60 min and (c) plasma-scan sintered (three dips, each scanned for 1 min). The plasma-scanned film has almost the same performance as that of the furnace-sintered film. This is an important result in terms of energetics. The furnace required 120 min to reach the sintering temperature and then the sample was sintered for a further 60 min, which corresponds to a total furnace usage of 180 min. Plasma scanning gave the same film properties in only 3 min, representing 60-times gain in process time efficiency.

Fig. 14 gives the potentiodynamic polarization curves of the stainless steel substrates with and without an aluminosilicate film, as measured in aqueous 3.5% NaCl solutions at room temperature (21 °C). The film under test was densified by plasma scanning. Fig. 14 reveals that the presence of the plasma-scanned aluminosilicate film on the stainless steel reduced the corrosion currents over a range of potentials. In support of this, the hydrochloric acid etchant used for the micrograph given in Fig. 11 produced no significant reaction or attack on the aluminosilicate film (on the left) in contrast to the deeply etched the stainless steel substrate (on the right). The results show that the plasma-scanned films confer substantial corrosion resistance on the substrate.

Oxidation resistance was assessed by isothermally heating both the coated and polished uncoated stainless steel samples to 900 °C in air for a series of times between 2 and 20 h. The film samples were prepared by three dips and plasma-scan sintering after each dip for 1 min. An argon + 6% hydrogen plasma was used with other parameters as given in Table 1. The weight gains during these tests were measured and reported in Table 2. The results show that the coated samples exhibited an order of magnitude less weight gain than the uncoated samples. This indicates that the plasma-scanned film provides substantial oxidation resistance to the stainless steel substrate.

The property evaluation tests therefore indicate that plasma-scan sintering of aluminosilicate films provides enhanced scratch, corrosion and oxidation resistance.

4. Conclusions

Plasma-scan sintering provides rapid heating and sintering for sol–gel films. The equilibrium sintering temperature for most samples can be reached in less than 1 min.

A process model has been developed and validated for the plasma-scan sintering process. The equilibrium temperature for a given scanning pattern can be predicted and controlled by the plasma gas composition and arc power.

Dense and crack-free aluminosilicate glass films have been successfully deposited on stainless steel using sol–gel and plasma-scan sintering at 600 °C for 1–3 min. The microstructure of plasma-scan sintered aluminosilicate films is similar to that of furnace-sintered films.

The critical thickness up to which crack-free films can be obtained is significantly lower for plasma-scan sintering than that for conventional furnace sintering. The current study shows that the critical thickness for plasma-scan sintering is 0.3 μm compared with 1.0 μm for furnace sintering.

Crack-free films above the critical thickness can be produced by multiple dipping to produce individual layers below the critical thickness and plasma scanning after each dip.

The aluminosilicate glass films on steel substrates sintered by plasma jet for 3 min at 600 °C showed the same scratch resistance as that of a film sintered in furnace for 60 min at 600 °C.

Aluminosilicate films prepared with three-dip and multiple plasma-scan sintering were shown to confer substantial scratch, corrosion and oxidation resistance to the substrate.

References

1. Wright, J. and Sommerdijk, N., *Sol–gel Materials Chemistry and Applications*. Wiley, New York, 2001.
2. Klein, L. C., *Sol–gel Technology for Thin Films, Fibers, Preforms, Electronics and Specialty Shapes*. Noyes Publications, Park Ridge, NJ, 1988.
3. Uhlmann, D. R. and Teowee, G., Sol–gel science and technology: current state and future prospects. *J. Sol–gel Sci. Technol.*, 1998, **13**, 153–162.
4. Yi, G. and Sayer, M., Sol–gel processing of complex oxide films. *Ceram. Bull.*, 1991, **70**, 1173–1179.
5. Turner, C. W., Sol–gel process-principles and applications. *Ceram. Bull.*, 1991, **70**, 1487–1490.
6. Atkinson, A. and Guppy, R. M., Mechanical stability of sol–gel films. *J. Mater. Sci.*, 1991, **26**, 3869.
7. Chena, B., Huanga, C. and Wu, L., Crack alleviation processing of lead zirconate titanate thin films deposited by sol–gel method. *Thin Solid Films*, 2003, **441**, 13–18.
8. Brunckov, H., Medvecky, L. and Mihalik, J., Effect of sintering conditions on the pyrochlore phase content in PMN–PFN ceramics prepared by sol–gel process. *J. Eur. Ceram. Soc.*, 2008, **28**, 123–131.
9. Liu, C., Nayak, P., Lin, Z. and Jeng, K., The effects of sintering temperature on preparation, resistivity, and thermopower of c-axis oriented $Ca_3Co_{3.95}Fe_{0.05}O_{9+\delta}$ films fabricated using sol–gel spin coating method. *Thin Solid Films*, 2008, **516**, 8564–8568.
10. Taylor, D. J and Fabes, B. D., Laser processing of sol–gel coatings. *J. Noncryst. Solids*, 1992, **147 & 148**, 457–462.
11. Lopatin, C. M., Alford, T. L., Pizziconi, V. B., Kuan, M. and Laursen, T., Ion-beam densification of hydroxyapatite thin films. *Nucl. Instrum. Methods B*, 1998, **145**, 522.
12. Scherer, G. W., Sintering of sol–gel films. *J. Sol–gel Sci. Technol.*, 1997, **8**, 353–363.
13. Wang, J., Binner, J., Pang, Y. and Vaidhyanathan, B., Microwave-enhanced densification of sol–gel alumina films. *Thin Solid Films*, 2008, **516**, 5996–6001.
14. Bao, Y., Gawne, D. T., Zhang, T., Qiu, Z. and Zhang, K., Influence of second phase on residual stress of plasma sprayed glass coatings. *Surf. Eng.*, 2000, **16**(6), 473–479.
15. Gawne, D. T., Zhang, T. and Liu, B., Computational analysis of the influence of a substrate, solid shield and gas shroud on the flow field of a plasma jet. *Surf. Coat. Technol.*, 2002, **153**(2–3), 138–147.
16. Nylen, P., Wigren, J., Pejryd, I. and Hansson, M., Modelling of coating thickness, heat transfer and fluid flow and its correlation with the TBC microstructure for a plasma sprayed gas turbine application. In *Thermal Spray: Meeting the Challenges of the 21st Century*, *vol. 1*, ed. C. Coddet. ASM, Ohio, USA, 1998, pp. 361–366.
17. Bao, Y., Zhang, T. and Gawne, D. T., Non-steady state heating of substrate and coating during thermal-spray deposition. *Surf. Coat. Technol.*, 2005, **194**, 82–90.
18. Zhang, T., Bao, Y. and Gawne, D. T., Process model of plasma enamelling. *J. Eur. Ceram. Soc.*, 2003, **23**, 1019–1026.
19. Fardad, M. A., Yeatman, E. M., Dawnay, E. J. C., Green, M. and Horowitz, F., Effects of H_2O on structure of acid-catalysed SiO_2 sol–gel films. *J. Noncryst. Solids*, 1995, **183**, 260–267.